RESEARCH ARTICLE

Nanoporous SiOx plasma polymer films as carrier for liquid-infused surfaces

Tobias Gergs[1] | Chiara Monti[2] | Sandra Gaiser[2] | Martin Amberg[2] |
Urs Schütz[2] | Thomas Mussenbrock[1] | Jan Trieschmann[3] |
Manfred Heuberger[2] | Dirk Hegemann[2]

[1]Applied Electrodynamics and Plasma Technology, Ruhr University Bochum, Bochum, Germany

[2]Swiss Federal Laboratories for Materials Science and Technology, Advanced Fibers, St. Gallen, Switzerland

[3]Department Theoretical Electrical Engineering, Kiel University, Kiel, Germany

Correspondence
Dirk Hegemann, Swiss Federal Laboratories for Materials Science and Technology, Advanced Fibers, St. Gallen, Switzerland.
Email: dirk.hegemann@empa.ch

Abstract

Liquid-infused surfaces are based upon the infusion of a liquid phase into a porous solid material to induce slippery and repellent character. In this context, porous SiOx plasma polymer films represent a relevant candidate for a robust nanoporous carrier layer. Intermittent low-pressure plasma etching of O_2/hexamethyldisiloxane-derived coatings is investigated to enhance the intrinsic porosity inherent to residual hydrocarbons in the silica matrix. Simulations of the resulting Si–O ring network structure using reactive molecular dynamics indicate formation of interconnected voids with Si–OH functionalized pore walls allowing water penetration with almost Fickian diffusive behavior. The corresponding porosity of up to 18%, well agreeing with simulations, Fourier-transform infrared spectroscopy, and ellipsometry measurements, was found to be suitable for the liquid infusion of poly-ethylene glycol molecules into about 80 nm thick SiOx films providing ongoing lubricating properties, thus revealing their suitability as liquid-infused surfaces.
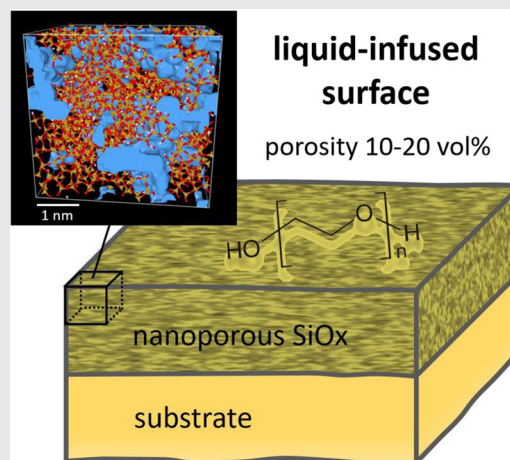
1 | INTRODUCTION

In the last decade, there has been intense research in developing liquid-infused surfaces, inspired by the antiwetting behavior of oil droplets on fish skin and the pitcher plant of the genus Nepenthes.[1–3] This strategy is based upon infusing a barrier liquid phase into porous solid materials to induce slippery and repellent character toward other liquids of differing polarity. Contrarily to micro/nanostructured surfaces in the so-called Cassie–Wenzel state, the intermediary liquid layer in liquid-infused systems separates the solid substrate from the second liquid or counterpart by means of preventing direct contact among them.[4] A wide range of attractive properties in applications is thus offered, including antibiofouling in both medical and marine environments, non-wetting or drag-reducing properties, anti-icing properties, and droplet manipulation.[3–5] However, many of these examples still show limitations in real-life applications due to their complex fabrication, draining, and wear damage.[5,6]

For this reason, we aim to study the possibility of developing liquid-infused surfaces by using a well-known and relatively cheap material such as organo-silica (SiO:CH). Such SiOx coatings can be deposited by plasma polymerization using organosilicon compounds such as hexamethyldisiloxane (HMDSO) at low substrate temperature yielding an amorphous structure containing residual organic groups, pores, and end groups within a Si–O network. Film properties can largely be defined regarding hardness, density, porosity, and wettability, mainly depending on their residual organic (hydrocarbon) content.[7,8] While organic/inorganic multilayers of SiOx found applications in the packaging field acting as barrier coatings,[9] Plasma polymerized SiOx films have also been widely studied as low dielectric constant materials, compared to pure silica, for advanced electronic devices.[10] The crucial element and property in the decrease of the dielectric constant, is the incorporation of carbon and hydrogen in the silicon oxide network, leading to an intrinsic porosity of nanodimensional size in the material.[11,12] However, such porous organosilicate glass (POG) layers as used for low-k dielectrics require air curing (400°C) to enhance their porosity,[13] which excludes deposition on polymer substrates.

We have developed a special understanding of plasma deposition conditions involving gas phase and surface processes in intermittent combination with oxygen plasma etching to remove the organic hydrocarbon content.[14,15] Along these lines, we introduce plasma deposition/plasma etching cycles to deposit SiOx films with enhanced porosity from Ar/O$_2$/HMDSO plasmas with intermittent Ar/O$_2$ plasma etching to remove

residual hydrocarbons. The obtained silica-like network is porous and chemically stable, it has good mechanical properties and wear resistance, while it is transparent—all properties of interest in many applications.[16] Liquid infusion on optimized SiOx films regarding porosity is first studied by diffusion of water through the pores, and later using a lubricant, polyethylene glycol, by showing its effect on surface friction.

To accompany the experimental work, the formation of pores in SiOx was also simulated using reactive molecular dynamics (RMD). The diffusion of H$_2$O molecules through amorphous silica is limited by the material's Si–O ring network structure. Rings with 6 or more Si–O members are required to allow for the diffusion of water molecules at room temperature.[17,18] Hence, the diffusion and uptake of water is enhanced for films with larger rings, that is, porous films, which is, therefore, a reasonable indication for the diffusive property of a particular SiOx system. Aside from the total porosity, the interconnection of the pores determines how water migrates and thus infuses the surface. However, the precise pore interconnectivity and underlying ring structure can hardly be characterized experimentally. Hence, RMD simulations are performed to support the experimental findings for amorphous silica (a-SiO$_2$), hydrogenated amorphous silica (a-SiO$_{2.2}$H$_{0.4}$), and nanoporous hydrogenated amorphous silica (a-SiO$_{2.2}$H$_{0.4}^P$). The structural changes in amorphous silica due to hydrolysis reactions (silanol groups) as well as due to an enhanced porosity are investigated.

2 | METHODS

2.1 | Experimental

2.1.1 | Plasma deposition of SiOx films

The plasma deposition and etching experiments were conducted in one of the four chambers of the large web coater at Empa.[19] The chamber with a volume of ~14 L contains a capacitively coupled, radio frequency-driven electrode of $21 \times 70 \, cm^2$ with 9 cm distance from the (larger) chamber wall. A gas showerhead facing the electrode enabled homogeneous plasma treatment conditions. The used substrates, silicon wafer (ellipsometry), aluminum foil (attenuated total reflection Fourier-transform infrared spectroscopy [ATR-FTIR]), and polymer foil (water sorption and friction tests), were mounted on the driven electrode. Evacuation enabled a base pressure of 10^{-4} Pa. The monomer HMDSO (purchased from Fluka), the carrier gas argon, and the reactive gas oxygen (purchased from Carbagas) were mixed and

introduced into the reactor by the gas showerhead. The liquid HMDSO was vaporized at reduced pressure and a temperature of 40°C and fed to the reactor via a thermostabilized mass flow controller (43°C).

Before deposition, the substrates were cleaned for 5 min by Ar/O_2 plasma (80/20 sccm) at 200 W applied power and 10 Pa pressure. For the deposition of dense amorphous SiO_2-like films as reference (SiO_2—ref.), an O_2/HMDSO ratio of 60/3 sccm was adjusted with 300 W and 4 Pa, while all other depositions used an O_2/HMDSO ratio of 40/4 sccm with 20 sccm of Ar addition at 100 W and 7 Pa resulting in amorphous films with about 15at% hydrocarbons (named SiOx).[20] For plasma etching of the residual CH content, the HMDSO flow rate was interrupted, while leaving the plasma on; etching power was adjusted to 100 W (SiOx_100W), 300 W (SiOx_300W), and 400 W (SiOx_400W). Five plasma deposition/etching cycles were performed with 1 min deposition and 5 min etching each, yielding a film thickness of ~80 nm. Note that the selection of a low HMDSO flow rate with a large deposition area resulted in rather low absolute deposition rates allowing a well-controlled film thickness in the nm-range, while assuring a high conversion of monomer into deposit.[14] Substrate temperature remained below 70°C for all conditions.

2.1.2 | ATR-FTIR measurements

The film composition was assessed by Fourier Transform Infrared Spectroscopy (Varian 640-IR, Agilent Technologies) by depositing the coatings on aluminum foils. The coated foils were smoothly contacted to a crystal using the ATR mode. The IR beam is directed onto the optically dense crystal having a high refractive index at a certain angle. This internal reflectance creates an evanescent wave that extends beyond the surface of the crystal into the sample yielding attenuation in regions of the IR spectrum where the sample absorbs energy, which is measured over the wavelength region of 650–4000 cm^{-1} with 2 cm^{-1} resolution. Note that ATR spectra have stronger absorbance bands at smaller wavenumbers than at larger wavenumbers compared to normal FTIR transmittance spectra.

2.1.3 | Ellipsometry

Deposited films on silicon wafers were analyzed by using the ellipsometer Nanofilm_EP4 (Accurion). Data were recorded at a constant wavelength of 658 nm by changing the angle of incidence from 55° to 80° to include the Brewster angle, that is, the angle of incidence at which

light with a particular polarization is perfectly transmitted through a transparent dielectric surface with no reflection. To gain information about porosity, the volume averaging theory (VAT) was applied as effective medium approximation using known film thickness by profilometry (Veeco, Dektak 150).[21]

2.1.4 | Water sorption

To study the diffusion process through the plasma coatings, the SiOx films were deposited on both sides of a recycled polyethylene terephthalate (rPET) sheet (thickness of ~200 μm, area of 7.5×7.5 cm^2) having a glass transition temperature of 75°C. As PET is known to be considerably hygroscopic, the kinetics of water sorption into the polymer sheet was determined gravimetrically over time with the samples fully submerged in water at 23°C. For weighing using a microbalance (Mettler Toledo XS204) with an accuracy of 0.1 mg, samples were removed and blown dry. For each measurement point, one sample was used. Before immersion, the samples were dried overnight in vacuum at a pressure of 10^{-4} Pa. Recycled PET sheets were measured as reference, and also with the four different SiOx plasma polymer films coated on both sides (seven samples each), starting the measurement right after venting.

2.1.5 | Friction tests

Friction tests were performed on a textile friction analyzer using a leather textile (Lorica©) as counterpart with a round contact area of 28.5 mm in diameter (6.4 cm^2).[22] During the test, the sample remains stationary while the textile counterpart on its metallic support is submitted to a reciprocating movement (1400 cycles). The friction force is measured by a quartz force sensor (Kistler, Type 9203) combined with a charge amplifier (Kistler, Typer 5011B) and sampled using a transient recorder PC-board (Bakker, Type BE490). Friction coefficients are determined for all sliding friction cycles. The following conditions were defined for the tests: a normal load of 5 N, resulting in a contact pressure of 4.7 kPa, and a stroke of 20 mm at a frequency of 1.25 Hz. All experiments took place at a temperature of 23°C and a relative humidity of 65%. The samples were acclimatized for more than 24 h in the laboratory. Thin films of about 80 nm thickness were deposited on rPET foils, and analyzed before and after 24 h of infusion with polyethylene glycol (PEG 200, having a molar mass of 190–210 g mol^{-1}), as a common, ecofriendly lubricant.[23]

2.2 | Simulation

The open source molecular dynamics code LAMMPS is used in combination with the ReaxFF potential to construct and study the chosen silica systems (i.e., a-SiO$_2$, a-SiO$_{2.2}$H$_{0.4}$, and a-SiO$_{2.2}$H$_{0.4}$^{P}),[24–26] reflecting the Si–O network of the experimental coatings SiO$_2$, SiO$_x$, and SiO$_x$_100W. The ReaxFF potential has been used in various scenarios to investigate, for instance, the water silica interface, reaction, and diffusion.[27–31] The timestep for any simulation in this study is chosen to be 0.2 fs. The Berendsen thermostat and barostat are applied during the system preparations unless stated otherwise.[32] The Nosé–Hoover chain thermostat and barostat implemented in LAMMPS are utilized for the final production runs.[24,25,33–37] All thermostats and barostats are set up with damping constants of 0.1 and 1 ps, respectively. The bulk modulus for the Berendsen barostat is 40 GPa.

At first, a-SiO$_2$ is prepared by applying a slightly altered procedure as proposed elsewhere.[27] A total of 1150 SiO$_2$ molecules are distributed randomly in a simulation box (4 nm × 4 nm × 4 nm), initializing the system with a mass density of 2.2 g cm^{-3}. The atom configuration is then relaxed by performing the conjugate gradient energy minimization implemented in LAMMPS up to an energy tolerance of 10^{-8} kcal/mol to avoid artificially high forces.[24,25] The system is then coupled to a thermostat at 4000 K and evolved in time for 50 ps. Afterward, the temperature is gradually reduced down to 293 K with a cooling rate of 10 K ps^{-1}, that is, for 371 ps. This quenching rate is 2.5 times slower than originally proposed to account for the equilibration of hydrolysis reactions later on.[27] The system is annealed at 4000 K and 1 atm by applying a thermostat and barostat for 100 ps. Subsequently, the temperature is cooled down to 293 K with a quenching rate of 10 K ps^{-1} while still being coupled to the barostat (adjusting the cell volume). Afterward, the simulation is run at 293 K and 1 atm for another 100 ps. The final production run is performed under the same conditions for 400 ps, out of which the last 200 ps are used to average the mass density, finally yielding 2.24 g cm^{-3}. Due to the applied relaxation of the system, the final box size is slightly different than the initial size.

For the a-SiO$_{2.2}$H$_{0.4}$ system, 1150 SiO$_2$ and 230 H$_2$O molecules are distributed randomly in the beginning. Aside from that, the same procedure as described above is applied. Thirteen H$_2$O molecules have not formed any silanol groups and are therefore removed. The final production run at 293 K and 1 atm is performed for 500 ps, out of which the last 200 ps are used to average the mass density, here, 1.89 g/cm^{-3}. The obtained

a-SiO$_{2.2}$H$_{0.4}$ configuration is used in the following to prepare the nanoporous a-SiO$_{2.2}$H$_{0.4}$^{P} by applying the volume-scaling method.[38,39] This technique is argued to be more suitable for imitating nanoporosity caused by CVD processes while charge-scaling provides a decent approximation in case of sol-gel-processed silica.[40,41] The targeted density of 1.7 g cm^{-3} is setup by iteratively performing three tasks: (i) increase the volume by 20% (isotropic strain), (ii) run the simulation for 100 ps at 293 K, which is achieved by using the Nosé-Hoover chain thermostat, and (iii) perform a simulation for 100 ps while the system is coupled to the Nosé-Hoover chain thermostat at 293 K and barostat at 1 atm. If the obtained and desired mass density differs from each other, the resultant atom configuration after step (ii) is reloaded to continue with step (i). After four iterations this loop is terminated. The final production run consists of a continuous simulation at 293 K and 1 atm over the course of 500 ps, out of which 200 ps are used to average the mass density reaching 1.71 g cm^{-3}.

The Si–O network topology of all three cases are characterized by using the R.I.N.G.S. code, which is used to compute bond properties (e.g., average coordination for each species), bond angle distributions, and most importantly the ring statistics by means of the connectivity profile for rings with up to 20 Si–O members.[42] The connectivity profile is described by four properties: (i) the number of rings with n Si–O members divided by the total number of nodes (atoms) $R_C(n)$, (ii) the fraction of nodes at the origin of at least one ring with n Si–O members $P_N(n)$, (iii) the proportion of nodes for which the rings with n Si–O members are the shortest closed paths $P_{min}(n)$, and (iv) the fraction of nodes for which the rings with n Si–O members are the longest closed paths $P_{max}(n)$.[43–45] Any ring has to fulfill the strong rings criterion, that is, it cannot be described by combining any set of smaller rings.[46,47]

The porosity and pore distribution are computed in a similar way as the accessible surface area is determined.[48] A grid with 200 × 200 × 200 bins is used to subdivide the simulation cell. Each grid point represents a probe H$_2$O molecule with a radius of 1.4 Å. The van der Waals radii 1.1, 1.52, and 2.1 Å are used for H, O, and Si, respectively.[49] A loop through all atoms is then used to remove any overlapping probe H$_2$O molecules, that is, the particular interatomic distance is less than the sum of the individual van der Waals and H$_2$O radius. Periodic boundary conditions are taken into account by expanding the relevant regions and eventually remapping them. The grid points of the remaining probe H$_2$O molecules are postprocessed and smoothed by utilizing the alpha-shape algorithm implemented in OVITO with a probe sphere radius of 0.3 Å (approximately 1.5× bin
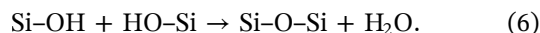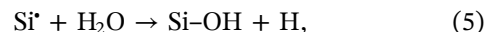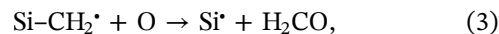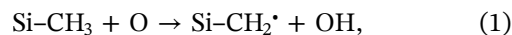
width).[50,51] As a result, the volume of each individual pore can be obtained and set into proportion to the simulation cell volume to determine the respective contribution to the net porosity of the system. However, this static approach neglects the plastic deformation during water uptake which eventually facilitates the diffusion of H_2O molecules through silica.[52] Hence, the here calculated porosity may rather be thought of as the lower limit. The negligence of further hydrolysis reactions during water uptake is justified due to their inactivity at room temperature.[28]

3 | RESULTS AND DISCUSSION

3.1 | Selection of process parameters

SiO_2-like plasma polymer films (PPFs) with high gas permeation barrier performance can be deposited from O_2/HMDSO plasmas at sufficiently high oxygen partial pressure and ion bombardment.[53] As reference, SiO_2 PPFs were thus deposited with an O_2/HMDSO ratio of 60/3 sccm (300 W, 4 Pa) at the RF-driven electrode of the referenced large CCP reactor (deposition rate of ~7.3 nm min^{-1}). A film density of $2.2 \pm 0.1 \, \text{g cm}^{-3}$ was derived, while the porosity is assumed to be negligible. Reducing the oxygen partial pressure and ion bombardment (by power and pressure variation), the deposition of less dense SiOx PPFs have been thoroughly studied in previous work using O_2/HMDSO of 40/4 sccm (100 W, 7 Pa, with 20 sccm Ar admixture).[15,20] Ar admixture supports fragmentation, oxidation, and deposition of less dense SiOx at moderate ion bombardment conditions.[54] Such films have a specific density of $1.9 \pm 0.1 \, \text{g cm}^{-3}$ with a chemical composition of $SiO_{1.9-2.0}C_{0.4-0.5}$ indicating residual hydrocarbons. Note that the CH content does not simply replace O in Si–O–Si by –CH_2 groups. To explain the observed composition, terminal groups such as Si–OH, Si–CH_3 and Si–$CH_2^{\bullet}$ besides Si–CH_2–CH_2–Si have to be assumed.[53,55,56] Most of all, the interaction with airborne atmospheric water supports the postplasma formation of silanol groups.[57] Hence, the formation of voids yielding porosity in the SiOx films can be expected also allowing water penetration. Neutron reflectometry (NR) measurements revealed that water initially diffused quickly into the coating during the first few hours, while it noticeably slowed down for >4 h of immersion by comparing dry samples with samples stored for different times in D_2O, yielding a water volume fraction of ~10%.[20,58] The porosity in SiOx can further be enhanced by plasma postoxidation yielding hydrocarbon removal by etching and further formation of Si–OH, while the Si–O–Si network is largely maintained.

In a simplified way, the following reactions are mainly responsible for etching and oxidation[59–61]:

$$\text{Si–CH}_3 + \text{O} \rightarrow \text{Si–CH}_2^{\bullet} + \text{OH}, \quad (1)$$

$$\text{Si–CH}_3 + \text{OH} \rightarrow \text{Si–CH}_2^{\bullet} + \text{H}_2\text{O}, \quad (2)$$

$$\text{Si–CH}_2^{\bullet} + \text{O} \rightarrow \text{Si}^{\bullet} + \text{H}_2\text{CO}, \quad (3)$$

$$\text{Si}^{\bullet} + \text{O} \rightarrow \text{Si–O}, \quad (4)$$

$$\text{Si}^{\bullet} + \text{H}_2\text{O} \rightarrow \text{Si–OH} + \text{H}, \quad (5)$$

$$\text{Si–OH} + \text{HO–Si} \rightarrow \text{Si–O–Si} + \text{H}_2\text{O}. \quad (6)$$

Therefore, O_2/Ar plasma etching (40/20 sccm, 100 W, 7 Pa) has previously been introduced to increase porosity after depositing the SiOx film as before.[15] The hydrocarbon etching resulted in chemical composition of $SiO_{2.2}$ with low, negligible carbon content indicating the incorporation of up to 10% Si–OH ($[SiO_2]_{0.9}\cdot[Si(OH)_4]_{0.1}$). The film density was reduced to $1.7 \pm 0.1 \, \text{g cm}^{-3}$ after plasma etching. Accordingly, enhanced water diffusion was observed by NR compared to SiOx.[15] Simulation results showed that demethylation is highly effective down to a depth of at least 15 nm for Ar/O_2 plasma etching of porous SiOCH.[59] To deposit thicker SiOx films of around 80 nm with enhanced porosity, named SiOx_100W, five deposition/etching cycles were thus applied using 1 min deposition (with a deposition rate of ~17 nm min^{-1}) and 5 min etching at maintained power of 100 W by intermitting the HMDSO gas flow. In the same way, the etching power was increased to 300 and 400 W during the etching cycles yielding SiOx_300W and SiOx_400W samples, respectively. A slightly lowered density of $1.6 \pm 0.1 \, \text{g cm}^{-3}$ was determined for etching cycles using 400 W. The latter is the maximum power that can be applied to avoid damage of polymer substrates by enhanced temperatures, that is, to stay below 70°C. Note that the overall film thickness was maintained despite the etching procedure, indicating solely hydrocarbon etching within a stable Si–O network. Film properties are summarized in Table 1.

ATR-FTIR spectra of the four different SiOx PPFs are shown in Figure 1. The features at 815 (symmetric), 1055 (asymmetric, transversal optical [TO] mode) and around 1200 cm^{-1} (asymmetric, longitudinal optical [LO] mode) correspond to the fundamental Si–O–Si bond stretching vibrations.[62,63] The peak at 815 cm^{-1}, however, can overlap with Si–OH stretching vibrations.[53] Further signatures of Si–OH and related adsorbed water

TABLE 1 Conditions and properties of experimentally deposited SiOx plasma polymer films compared to the results obtained by simulation

Experiment	O_2/HMDSO ratio; etching power	Density (g cm^{-3})	Porosity (%) ellips./sorption	Simulation	Density (g cm^{-3})	Porosity (%) sim.
SiO$_2$—ref.	60/3 sccm; none	2.2 ± 0.1	~0	a-SiO$_2$	2.24	0.5
SiOx	40/4 sccm; none	1.9 ± 0.1	>4/9.5 ± 2	a-SiO$_{2.2}$H$_{0.4}$	1.89	4.9
SiOx_100W	40/4 sccm; 100 W	1.7 ± 0.1	11 ± 2/11.5 ± 2	a-SiO$_{2.2}$H$_{0.4}$^{P}	1.71	10.4
SiOx_300W	40/4 sccm; 300 W	1.7 ± 0.1	12 ± 2/15.5 ± 2			
SiOx_400W	40/4 sccm; 400 W	1.6 ± 0.1	16 ± 2/17.5 ± 2			

Note: Obtained porosities using ellipsometry (ellips.), water sorption kinetics (sorption), and simulation (sim.) are summarized.
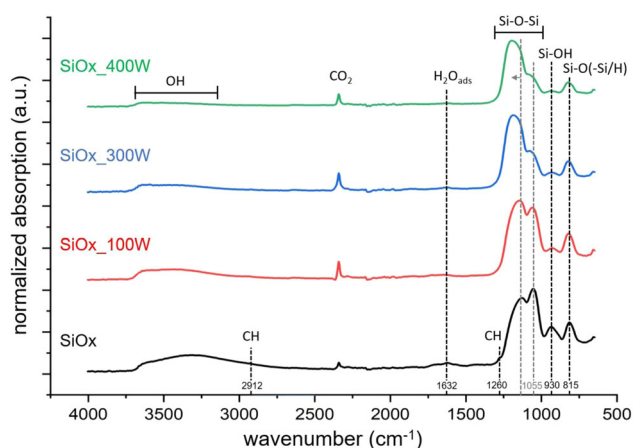

FIGURE 1 Attenuated total reflection Fourier-transform infrared spectroscopy spectra of SiOx coatings using Ar/O$_2$ plasma etching cycles of different power. Etching effects are mainly seen by a shift within the Si–O–Si region at 1000–1250 cm^{-1} (asymmetrical stretching). The peak at 2350 cm^{-1} corresponds to asymmetric stretching vibrations of gaseous CO$_2$

molecules can be detected at 930 and 1632 cm^{-1} as well as by the broadband between 3200 and 3650 cm^{-1}.[53,63,64] Even the non-etched SiOx film reveals only weak bands of residual hydrocarbons at 1260 cm^{-1}, corresponding to Si–CH$_3$ vibrations, and at 2912 cm^{-1}, corresponding to CH$_2$ stretching.[55] However, the region around 1000–1100 cm^{-1} might overlap with –CH$_2$—wagging vibrations in Si–CH$_2$–Si and Si–CH$_2$–CH$_2$–Si, which might also account for the weak absorption at 1350–1440 cm^{-1}.[55,65] Distinct changes upon etching with increasing power are seen in the LO–TO splitting of the Si–O–Si stretching vibration signal, mainly by the reduction of the TO peak intensity (1055 cm^{-1}), which might be related to oxidation and hydrocarbon removal but also to an increase of porosity.[66–68] In agreement, the peak position of the LO peak intensity (~1210 cm^{-1}) indicates a porous structure and the slight blue shift to higher wavenumbers with etching power points to increasing relaxation of the silica matrix.[66,69]

Furthermore, the intensity of the band around 3200 cm^{-1} decreased upon plasma etching, which could be explained by secondary condensation reactions of silanols with water to form siloxane bonds agreeing with the reduced peak at 930 cm^{-1}.[20,65] Note that we exclude formation of silicon oxycarbides during plasma oxidation due to low substrate temperature (<70°C), low residual carbon content (<5 at%), and the known film structure of organosilicon-derived SiOx films (free of C–O bonds).[70,71]

3.2 | Assessment of film porosity by simulation

To gain a better understanding of the porous structure in SiOx coatings, simulation of films with different densities was performed. An amorphous silica a-SiO$_2$ was considered as reference. The experimental SiOx coating with the complex chemical composition of SiO$_{1.9-2.0}$C$_{0.4-0.5}$ is represented by a-SiO$_{2.2}$H$_{0.4}$, that is, all Si–CH$_2$ and Si–CH$_3$ groups are formally replaced by Si–OH to simplify the simulation and to allow a direct comparison with the less dense, plasma-oxidized SiOx_100W film of composition a-SiO$_{2.2}$H$_{0.4}$^{P}, where the superscript "p" indicates the enhanced porosity. The adjusted mass densities for a-SiO$_2$, a-SiO$_{2.2}$H$_{0.4}$, and a-SiO$_{2.2}$H$_{0.4}$^{P} are 2.24, 1.89, and 1.71 g cm^{-3}, respectively, matching with the experimental ones (Table 1). The corresponding atom configurations are depicted in Figure 2.

The average Si coordination number (CN) in a-SiO$_2$ of 3.98 is slightly increased up to 3.99 due to the additional oxygen in a-SiO$_{2.2}$H$_{0.4}$ and eventually decreased down to 3.93 due to the strain-induced Si–O bond breaking during the formation of a-SiO$_{2.2}$H$_{0.4}$^{P}. The composition of the mean O CN in a-SiO$_2$ of 1.99 (100% O–Si) is changed to 2.00 (91.36% O–Si and 8.64% O–H) when hydrolysis reactions cause the formation of silanol groups during the preparation of a-SiO$_{2.2}$H$_{0.4}$. 0.35% of the O–Si bonds are replaced by O–H bonds when the
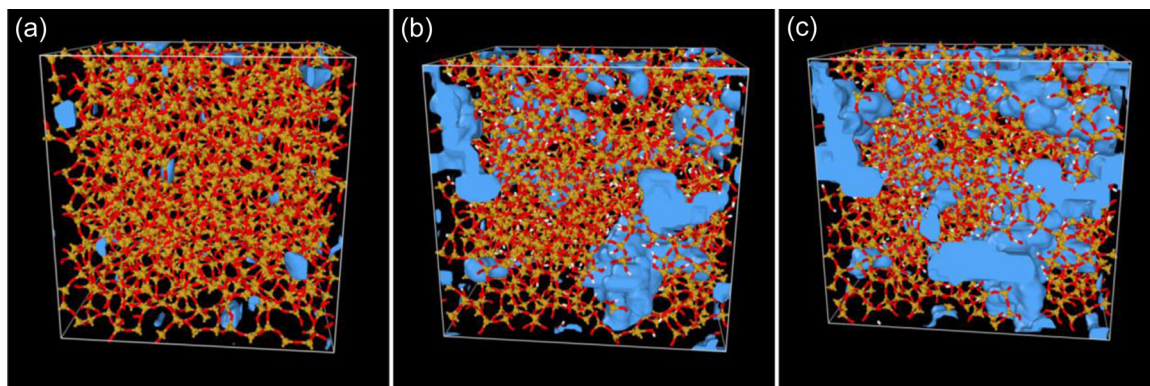
FIGURE 2 Atom configurations for (a) a-SiO$_2$, box size 3.65 nm × 3.75 nm x 3.75 nm, (b) a-SiO$_{2.2}$H$_{0.4}$, 3.90 × 4.14 × 3.97, and (c) a-SiO$_{2.2}$H$_{0.4}$^{P}, 4.06 × 4.33 × 4.06. White, red, and yellow indicate H, O, and Si atoms, respectively. Blue regions highlight the particular nanopore distribution. The atom configurations have been rendered with OVITO[50]
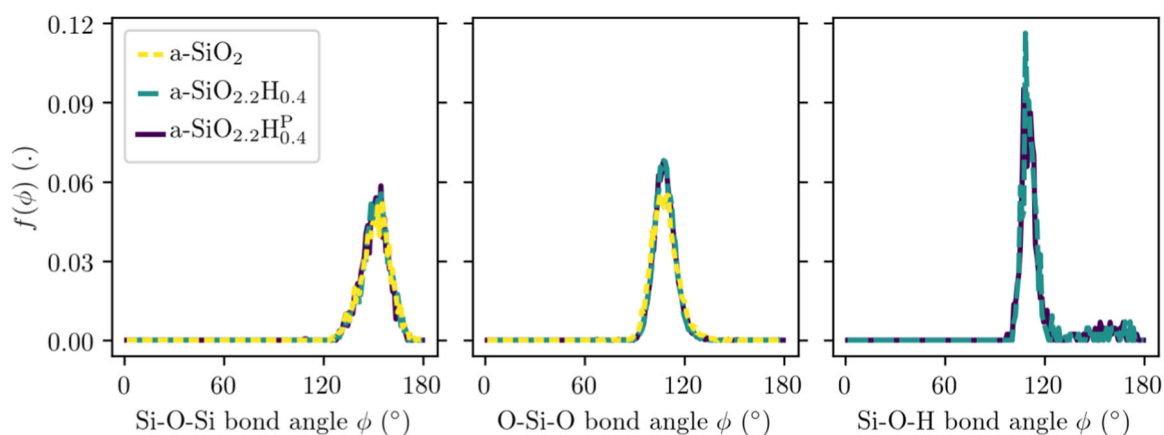

FIGURE 3 Si–O–Si, O–Si–O and Si–O–H bond angle distributions for a-SiO$_2$, a-SiO$_{2.2}$H$_{0.4}$, and a-SiO$_{2.2}$H$_{0.4}$^{P}

porosity of the system is further increased for a-SiO$_{2.2}$H$_{0.4}$^{P} showing pore dimensions of around 1 nm. This leads to an over coordination for a few H atoms (mean CN: 1.03), whereas all H atoms in a-SiO$_{2.2}$H$_{0.4}$ are bound to exactly one O atom (mean CN: 1.00). The individual defects of amorphous silica are described in detail elsewhere.[72]

While the bond configurations of the three systems differ from each other, no significant change in the Si–O–Si, O–Si–O, and Si–O–H bond angle distributions are found (Figure 3). But the Si–O–Si and O–Si–O peak bond angles 152.5° and 107.5° are in good agreement with the experimental values for amorphous silica (i.e., 151.0° and 109.4–109.5°, respectively).[73–77]

The analysis of the Si–O ring network topology by means of the connectivity profile is presented in Figure 4. The corresponding methodology and properties (i.e., R_C, P_N, P_{max}, P_{min}) are described in Section 2.2. Rings with 6 or more Si–O members allow for the diffusion of H$_2$O molecules at room temperature (blue-colored area).[17,18]

Figure 4a shows that for all three materials rings with seven Si–O members are the most dominant ring structure, which has been reported previously for dense and nanoporous silica.[41] However, the hydrolysis reactions and resultant silanol groups in a-SiO$_{2.2}$H$_{0.4}$ and a-SiO$_{2.2}$H$_{0.4}$^{P} reduce their numbers by a factor of 1.65 and 1.85, respectively. Furthermore, a more pronounced tail in the R_C distribution for ring sizes greater than 8 is established. This change is likely to facilitate H$_2$O diffusion.

A similar but less distinct trend can be observed for the P_N distributions, which are shown in Figure 4b. The majority of all Si and O atoms (i.e., a-SiO$_2$: 58%, a-SiO$_{2.2}$H$_{0.4}$: 39%, a-SiO$_{2.2}$H$_{0.4}$^{P}: 37%) are at least once at the origin of a ring with five Si–O members. Changes of P_{max} and P_{min} (Figures 4c,d, respectively) are well suited to highlight changes in the ring structure which are less frequent and may otherwise be overlooked. All materials provide almost identical P_{max} and P_{min} curves for rings which have less than seven Si–O members.
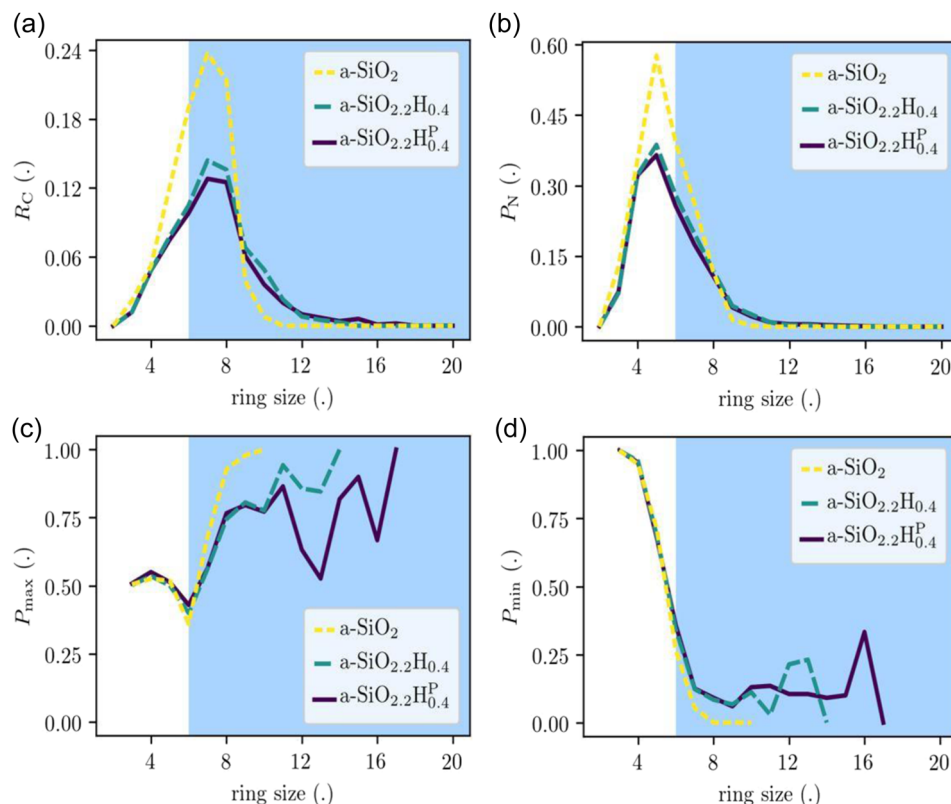
FIGURE 4 Connectivity profile for a-SiO$_2$, a-SiO$_{2.2}$H$_{0.4}$, and a-SiO$_{2.2}$H$_{0.4}$^{P}, which consists of (a) R_C, (b) P_N, (c) P_{max}, and (d) P_{min}. The blue region highlights rings with equal to or more than six Si–O members

However, there is a distinct difference between these systems for greater ring sizes. The introduction of silanol groups (hydrolysis reactions) disrupts the amorphous Si–O ring network, raising the size of the largest Si–O ring from 10 to 14. Increasing the porosity has a similar effect due to the accompanied Si–O bond breaking, discussed previously. The greatest ring size is found to be 17. It is to be expected that these large rings represent the longest closed paths for various atoms (i.e., P_{max}). However, these rings are also equal to the shortest closed path for up to approximately 25% of the atoms (i.e., P_{min}). This local maximum in the tail of P_{min} distribution can be attributed to corresponding nanopores with around 1 nm diameter.

The pores of all three atom configurations are shown in Figure 2. The resulting porosity of a-SiO$_2$ is 0.5%. The hydrolysis reactions (silanol groups) in a-SiO$_{2.2}$H$_{0.4}$ alter the amorphous silica structure in a way that facilitates H$_2$O diffusion while at the same time increasing the potential water uptake to about 4.9%. The greatest nanopore contributes 44.9% to the net porosity, which readily increases water diffusivity. The observed porosity of a-SiO$_{2.2}$H$_{0.4}$^{P} is 10.4%. The bond breaking and inherent ring structure modifications cause the formation of even larger nanopores. A total of 95.2% of the material's porosity is represented by one interconnected nanopore, providing diffusion channels for the transport of H$_2$O molecules. Keeping in mind that the assessment of porosity by simulation represents rather the lower limit, the obtained porosity values agree well with the experimental findings, as discussed in the following (Table 1).

3.3 | Assessment of film porosity by ellipsometry

Porosity is an essential characteristic that affects film properties such as the refractive index. For this reason, the refractive index analysis by ellipsometry was chosen to evaluate the effective nanoporosity of SiOx coatings. The refractive index measures the bending of a ray of light when passing from one medium to another. For porous materials it is possible to approximate the material as a composite made of a condensed phase (the pristine material) and a dispersed phase (a fluid, typically air). This approximation is called effective medium approximation (EMA) and treats heterogeneous materials, such as porous materials, as homogeneous materials with some effective properties.[78] Accordingly,

the refractive index of heterogeneous media can be predicted based on the optical properties and volume fractions of its constituent materials, assumed to be known. For porous materials, this approach is valid if the pore size is much smaller than the wavelength λ of incident light so that scattering by pores can be ignored. In addition, the film should be thick compared to the pore size to consider a sufficiently large representative volume of the film, which is fulfilled for nanoporous SiOx coatings. In this case, the most commonly used EMA as used in this study is the VAT.[21] The VAT model expresses the effective refractive index $n_{eff,\lambda}$ of a non-absorbing two-phase composite as

$$n_{eff,\lambda}^2 = \phi n_{d,\lambda}^2 + (1 - \phi) n_{c,\lambda}^2, \tag{1'}$$

where ϕ is the total porosity, the subscript c refers to the continuous phase (e.g., silica) and the subscript d refers to the dispersed phase (e.g., air or water). From Equation (1') it is possible to derive the porosity as follows:

$$\phi = \frac{n_{eff,\lambda}^2 - n_{c,\lambda}^2}{n_{d,\lambda}^2 - n_{c,\lambda}^2}. \tag{2'}$$

For the examined SiOx coatings the effective refractive index $n_{eff,\lambda}$ was calculated by ellipsometry with samples deposited on silicon wafers by knowing the thickness from profilometry measurements, leaving the refractive index as the only fitting parameter. From the results shown in Figure 5, it can be noted that by increasing the etching power, the refractive index decreases indicative of nanoporosity. Using the refractive index of the SiO2-like reference coating, $n_{c,\lambda} = 1.503$, and for air, $n_{d,\lambda} = 1$, the porosity of the coatings, defined as the fraction of voids, can be calculated according to Equation (2'). For the plasma-etched films it can be assumed that the residual hydrocarbon content of SiOx was largely removed and the VAT model is valid. For SiOx_100W, SiOx_300W, and SiOx_400W, respectively, an increasing porosity from 11% to about 16% with etching power was calculated (Table 1). Note that the value for SiOx_100W agrees well with the porosity as obtained by simulation. For SiOx that contains about 15 at% residual hydrocarbons,[15,20] the porosity analysis, however, is more of qualitative nature. Since hydrocarbons in SiOx tend to increase the refractive index, countering the effect by the void fraction,[57] the calculated porosity of around 4% is thus an underestimation. However, the properties are close to the simulation of a dense silica phase containing voids by Si–OH (a-SiO2.2H0.4).

Comparing the refractive indexes of the coatings with fused silica ($n = 1.46$ at 658 nm wavelength), it is interesting to note that the measured values are comparable or even higher. The reason for this is
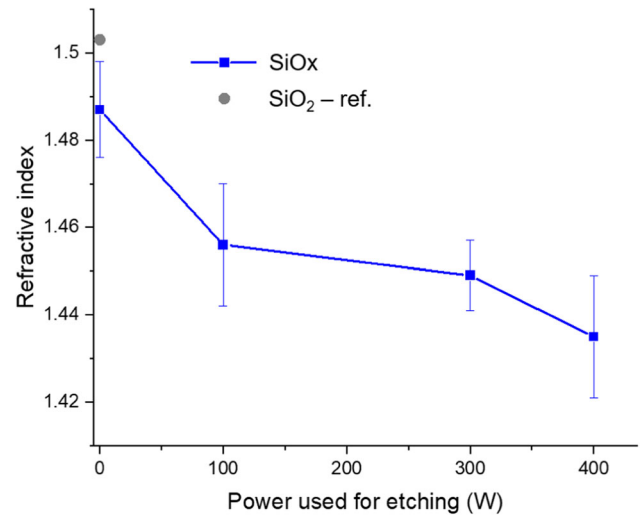

FIGURE 5 Determination of refractive index of SiOx coatings in air using ellipsometry. The refractive index depends on residual hydrocarbon content and porosity and thus on the applied intermittent etching conditions

quasi-instantaneous moisture absorption upon venting the plasma chamber consequently increasing the pore refractive index compared to 1 (air).[69] Therefore, fused silica has not been taken as a reference for the porosity calculation.

3.4 | Assessment of film porosity by water sorption

The diffusion of water through the different SiOx coatings was further assessed by gravimetrically determined water sorption kinetics using a plasma-coated hygroscopic substrate material. For this purpose, rPET sheets with a crystallinity of about 10% (thickness ~200 μm, area 7.5 × 7.5 cm^2, weight ~1.5 g) were used as substrate to be coated on both sides. Recycled polymers of low crystallinity are known to show enhanced water-absorbing capabilities due to shorter chain lengths and defects, whereby an almost Fickian diffusive behavior can be expected that can be assessed by water sorption kinetics.[79,80] For an isotropic material such as PET, the concentration-depending first and second Fick's laws of diffusion can be applied in their simplest form yielding the approximate solution for one-dimensional diffusion[81]:

$$\frac{m_t}{m_s} = 1 - \exp\left[-7.3\left(\frac{Dt}{h^2}\right)^{0.75}\right], \tag{3'}$$

where m_t is the mass of the solute at time t, m_s the mass of solute at saturation, D the diffusion coefficient, and h
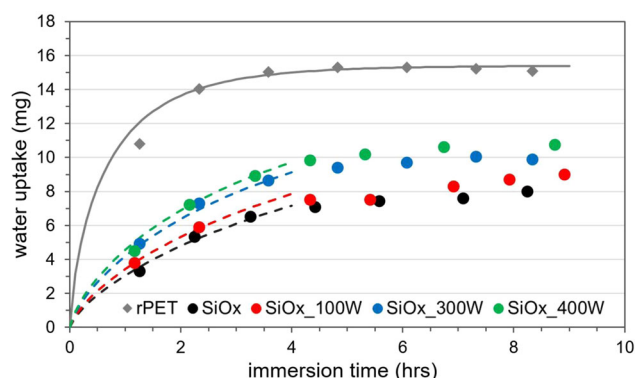
FIGURE 6 Gravimetric water uptake of 80 nm thick SiOx coatings deposited on both sides of rPET sheets using different etching conditions. The fitting according to Fick's law initially shows almost Fickian diffusive behavior, which is used to calculate porosity with respect to the uncoated rPET reference. rPET, recycled polyethylene terephthalate

the thickness of the sheet (200 μm). When the sheet is coated by a porous material, the effective diffusion coefficient, D_e, is reduced by the exposed area, here, the porosity, ϕ, and the tortuosity factor, τ[82]:

$$D_e = \frac{\phi}{\tau}D. \qquad (4')$$

At first, the water sorption kinetics by rPET were gravimetrically determined, reaching saturation (around 1 wt%) within a few hours (Figure 6). An almost Fickian diffusive behavior was observed yielding $D = 1.1 \pm 0.1$ μm^2 s^{-1} based on Equation (3'). This value is about double as reported for virgin PET with 10% crystallinity,[80] likely owing to the recycling process. D and m_s from rPET can then be used to fit the plasma-coated rPET sheets, which gives acceptable fitting over the first few hours of water sorption, while deviating at longer times. Porous SiOx readily takes up moisture from the atmosphere after plasma deposition that reacts to form silanols.[62,69] Consequently, a water droplet placed on the pristine coating completely wets within seconds, preventing further water contact angle analyses. Initially, the hygroscopic SiOx films with a pore dimension of around 1 nm might thus allow fast transport of water molecules when immersed in water, and water uptake is still governed by the free volume in the rPET sheet. Therefore, the observed almost Fickian diffusive behavior can be used to derive the porosity, and previous assumptions about the nonabsorbing behavior of the SiOx films as made for the assessment by ellipsometry seems to be validated. For many small interconnected voids as identified by simulation, the water molecules do not need to follow a tortuous path through the SiOx

coating to reach the polymer (different to barrier coatings). Furthermore, a pore dimension of 1 nm still allows bulk-like water in its center.[83,84] Hence, $\tau = 1$ can be assumed in Equation (4) and the porosity is simply given by D_e/D. Calculating values of 0.105, 0.125, 0.17, and 0.195 μm^2 s^{-1} for SiOx, SiOx_100W, SiOx_300W, and SiOx_400W, respectively, an increasing porosity from 9.5% up to about 17.5% with etching power was deduced (Table 1). Note that for SiOx a higher porosity of ~9.5% was obtained compared to ellipsometry, pointing to the importance of the residual hydrocarbon content, yet agreeing with previous NR results (~10%).[20]

Longer water interaction might result in water adsorption by hydrogen bonding within the porous SiOx film as described by a dual-mode adsorption model or yielding hydrolysis reactions as described by a reaction-diffusion model—both delaying water uptake with strongly reduced diffusion coefficients.[80,85] The same water diffusion characteristics in SiOx have been observed by NR.[20] While this behavior is of importance for SiOx barrier coatings exposed to water,[86] a further discussion is out of the scope of this paper. In agreement with simulation and ellipsometry, the simple assessment of porosity by water sorption kinetics demonstrates the feasibility to deposit highly porous SiOx films at low temperatures using intermittent Ar/O$_2$ etching.

3.5 | Infusion of liquids into porous SiOx films

Demonstrating that a polar liquid such as water can diffuse into the silica matrix of the porous SiOx plasma polymer films, the diffusion of polyethylene glycol (PEG), containing a polar oxygen and a nonpolar (CH$_2$)$_2$ group in each unit, might be supported, as well. PEG hydrogels are widely used as lubricating coating in aqueous and nonaqueous environments.[23,87] An appropriate lubricant is distinguished by a low vapor pressure, chemical inertness, and a suitable viscosity.[5] Therefore, liquid PEG 200 with a low molar mass of 190–210 g mol^{-1} was selected to investigate the potential of porous SiOx films as carrier layer for liquid-infused surfaces. As PEG is a polar molecule, it is expected that it wets the pore walls of the SiOx coatings. For plasma-etched SiOx coatings, it was indeed found that a droplet of PEG was taken up by the porous film within about 10 s—similarly as water droplets. To allow infusion into 80 nm thick SiOx films, deposited on aluminum foils (used for FTIR) and rPET foils (used for friction tests), the coated samples were left for 24 h in PEG. After removal, the surface of the samples were wiped with a wet tissue to eliminate surface residuals.
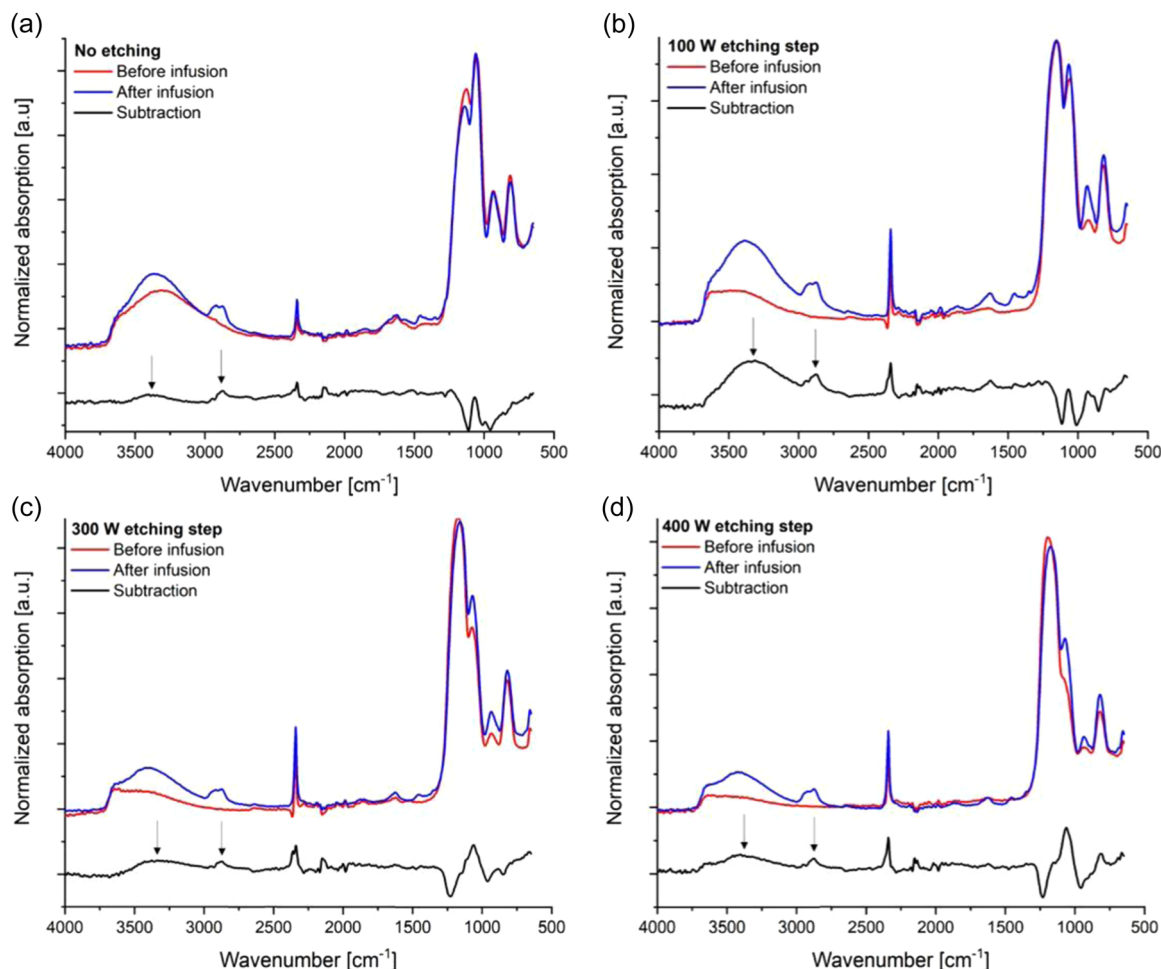
FIGURE 7 Aattenuated total reflection Fourier-transform infrared spectroscopy spectra of (a) SiOx, (b) SiOx_100W, (c) SiOx_300W, and (d) SiOx_400W with and without infusion of PEG. The black curves indicate the difference between the two measured spectra

ATR-FTIR analysis was performed to examine infusion by PEG into the four different SiOx coatings (Figure 7). Most of all, a broad peak at 3400–3500 cm^{-1} appeared, which corresponds to terminal hydroxyl groups of PEG,[88] and a peak around 2900 cm^{-1} indicating –CH$_2$ stretching. A related increase in the shoulder of the C–O stretching band (overlapping with the Si–O–Si band) at the lower wavenumber side (1060 cm^{-1}) is also characteristic for low molecular weight polyethylene glycol.[88] PEG infusion might thus be identified in all SiOx coatings, however, the observed signals might at least partly result from different levels of adsorbed PEG at the surface left after wiping. For SiOx_300W and SiOx_400W more pronounced changes in the Si–O–Si region of 1000–1250 cm^{-1} occurred. Note that these changes (red shift of LO peak intensity) are opposite to the effect by etching power. Identifying the Ar/O$_2$ plasma etching with increasing relaxation of the silica matrix, the PEG infusion might thus induce stress in the plasma polymer film, which might thus indicate the highest PEG uptake in SiOx_400W.

Based on the FTIR results, SiOx_100W and SiOx_400 W were selected for friction tests. The results for the dynamic and static coefficient of friction (CoF) against a leather textile over a range of 1400 cycles are presented in Figure 8.

The different levels of porosity correspond to different running-in behavior for the dry coatings without PEG infusion. The observed friction force for SiOx_100W is characteristic of dry friction partners having a small amount of surface contamination or adsorbed species, quickly worn away to cause a greater degree of adhesion and a rise in friction.[89] The shape of the friction curve of SiOx_400W, on the contrary, is common for non-lubricated partners in which the initial roughness of the surface produces a momentary rise in friction until surface conformity and smoothing occurs, reducing the friction. The PEG-infused surfaces showed a noticeably lowered CoF, initially comparable for the two examined porous carrier layers. The friction behavior of SiOx_100W, however, revealed a diminishing lubrication
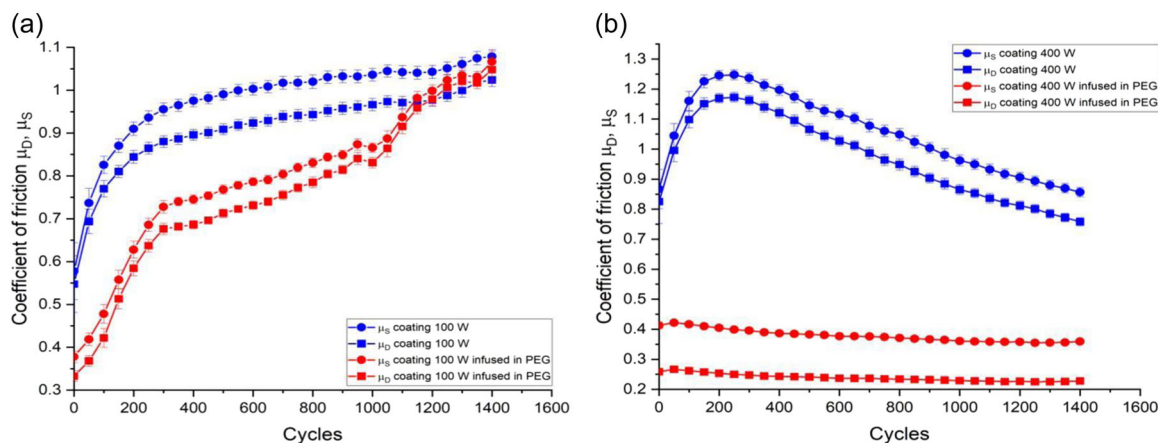
FIGURE 8 Static (circles) and dynamic (squares) coefficients of friction for the SiOx coatings, (a) with intermittent etching step of 100 W, and (b) 400 W. SiOx was deposited on recycled polyethylene terephthalate foils (blue curves) and infused with PEG (red curves). PEG, polyethylene glycol

effect, finally reaching the same level as the dry sample, which indicates displacement of lubricants present mainly at the surface. The highly porous surface of SiOx_400W, on the contrary, maintained a low CoF over long cycles, pointing to the infusion of PEG into the porous structure and steady release of lubricant. Note that water molecules, on the contrary, do not act as lubricant for this friction system.[22] The porous network was thus able to retain the infused PEG lubricant thanks to a strong interaction with the pore walls. In addition to their lubricating properties, surfaces decorated with hydrogels by means of plasma surface engineering are an emerging research topic for a broad field of applications.[90]

4 | CONCLUSIONS

Plasma polymerized SiOx coatings were investigated as a nanoporous carrier layer. SiOCH plasma polymers are known for their intrinsic porosity given by the incorporation of carbon and hydrogen in the silica matrix. To enhance porosity, the etching of such residual hydrocarbons by intermittent Ar/O_2 plasma etching was studied. Namely, SiOx deposition from an O_2/HMDSO plasma was intermitted by etching at different plasma power (without HMDSO in the gas phase) once a layer thickness of about 17 nm was reached, followed by further deposition/etching cycles. The observed removal of hydrocarbons left nanosized voids within the silicon oxide network enabling porous templates produced at low temperatures. Reactive molecular dynamics simulation was used to understand porous diffusion at the molecular level. The porous silica films form interconnected voids due to a Si–O ring network structure

containing six or more Si–O members that allow for the diffusion of water molecules at room temperature. The porosity was assessed with different techniques including ellipsometry and water sorption kinetic measurements. In agreement with the simulations, increasing plasma etching power resulted in enhanced porosity up to about 16%–18% leaving Si–OH functionalized pore walls. Water readily diffused into the porous network, initially showing Fickian diffusive behavior followed by increased interaction with the pore walls.

From this, PEG 200 with low molecular mass was selected as a lubricant to be infused into the SiOx plasma polymer films. FTIR results gave hints on the infusion of PEG, mainly for the highest etching power applied. Accordingly, PEG-infused SiOx_400W films revealed a noticeable lubricating performance when rubbing against a leather textile in a friction test without draining during the entire testing period. The interconnected porous network of the plasma-etched SiOx thin films thus fulfills the requirements to produce robust liquid-infused surfaces that can be deposited on various substrates including soft and temperature-sensitive materials.

CONFLICTS OF INTEREST
The authors declare no conflicts of interest.

DATA AVAILABILITY STATEMENT

The data that support the findings of this study are available from the corresponding author upon reasonable request.

ORCID

Tobias Gergs http://orcid.org/0000-0001-5041-2941
Sandra Gaiser http://orcid.org/0000-0001-9111-2953
Martin Amberg http://orcid.org/0000-0002-8900-8636
Thomas Mussenbrock http://orcid.org/0000-0001-6445-4990
Jan Trieschmann http://orcid.org/0000-0001-9136-8019
Manfred Heuberger http://orcid.org/0000-0001-5799-3785
Dirk Hegemann http://orcid.org/0000-0003-4226-9326

REFERENCES

[1] T. S. Wong, S. H. Kang, S. K. Y. Tang, E. J. Smythe, B. D. Hatton, A. Grinthal, J. Aizenberg, *Nature* **2011**, *477*, 443.
[2] P. Zhang, H. Chen, D. Zhang, *J. Bionic Eng.* **2015**, *12*, 79.
[3] M. Villegas, Y. Zhang, N. A. Jarad, L. Soleymani, T. F. Didar, *ACS Nano.* **2019**, *13*, 8517.
[4] E. Bormashenko, *Trans. R. Soc. A* **2019**, *377*, 20180264.
[5] S. Peppou-Chapman, J. K. Hong, A. Waterhouse, C. Neto, *Chem. Soc. Rev.* **2020**, *49*, 3688.
[6] J. S. Wexler, I. Jacobi, H. A. Stone, *Phys. Rev. Lett.* **2015**, *114*, 168301.
[7] D. Hegemann, H. Brunner, C. Oehr, *Surf. Coat. Technol.* **2003**, *174–175*, 253.
[8] A. S. M. de Freitas, C. C. Maciel, J. S. Rodrigues, R. P. Ribeiro, A. O. Delgado-Silva, E. C. Rangel, *Vacuum* **2021**, *194*, 110556.
[9] M. Jaritz, P. Alizadeh, S. Wilski, L. Kleines, R. Dahlmann, *Plasma. Process. Polym.* **2021**, *18*, e2100018.
[10] W. Volksen, R. D. Miller, G. Dubois, *Chem. Rev.* **2010**, *110*, 56.
[11] V. Purohit, E. Mielczarski, J. A. Mielczarski, L. Akesso, *Mater. Chem. Phys.* **2013**, *141*, 602.
[12] D. J. Michalak, J. M. Blackwell, J. M. Torres, A. Sengupta, L. E. Kreno, J. S. Clarke, D. Pantuso, *J. Mater. Res.* **2015**, *30*, 3363.
[13] M. Rasadujjaman, Y. Wang, L. Zhang, S. Naumov, A. G. Attallah, M. O. Liedke, N. Koehler, M. Redzheb, A. S. Vishnevskiy, D. S. Seregin, Y. Wu, J. Zhang, J. Leu, A. Wagner, K. A. Vorotilov, S. E. Schulz, M. R. Baklanov, *Micropor. Mesopor. Mat.* **2020**, *306*, 110434.
[14] D. Hegemann, E. Bülbül, B. Hanselmann, U. Schütz, M. Amberg, S. Gaiser, *Plasma. Process. Polym.* **2021**, *18*, e2000176.
[15] E. Bülbül, P. Rupper, T. Geue, L. Bernard, M. Heuberger, D. Hegemann, *ACS Appl. Mater. Interfaces* **2019**, *11*, 42760.
[16] C. Hoppe, F. Mitschker, L. Mai, M. O. Liedke, T. de, P. Arcos, A. Awakowicz, A. G. Devi, M. Attallah, A. Butterling, G. Wagner, G. Grundmeier, *Plasma. Process. Polym.* **2022**, *19*, e2100174.
[17] T. Bakos, S. N. Rashkeev, S. T. Pantelides, *Phys. Rev. Lett.* **2002**, *88*, 055508.
[18] T. Bakos, S. N. Rashkeev, S. T. Pantelides, *Phys. Rev. B.* **2004**, *69*, 195206.
[19] N. E. Blanchard, B. Hanselmann, J. Drosten, M. Heuberger, D. Hegemann, *Plasma Processes Polym.* **2015**, *12*, 32.
[20] N. E. Blanchard, V. V. Naik, T. Geue, O. Kahle, D. Hegemann, M. Heuberger, *Langmuir* **2015**, *31*, 12944.
[21] M. Braun, L. Pilon, *Thin Solid Films* **2006**, *496*, 505.
[22] E. Bertaux, E. Le Marec, D. Crespy, R. Rossi, D. Hegemann, *Surf. Coat. Technol.* **2009**, *204*, 165.
[23] Z. Han, C. Gan, X. Li, P. Feng, X. Ma, X. Fan, M. Zhu, *Tribol. Int.* **2021**, *161*, 107057.
[24] S. Plimpton, *J. Comput. Phys.* **1995**, *117*, 1.
[25] A. P. Thompson, H. M. Aktulga, R. Berger, D. S. Bolintineanu, W. M. Brown, P. S. Crozier, P. J. in't Veld, A. Kohlmeyer, S. G. Moore, T. D. Nguyen, R. Shan, M. J. Stevens, J. Tranchida, C. Trott, S. J. Plimpton, *Comput. Phys. Commun.* **2022**, *271*, 10817.
[26] N. Nayir, A. C. T. van Duin, S. Erkoc, *J. Phys. Chem. A* **2019**, *123*, 4303.
[27] J. C. Fogarty, H. M. Aktulga, A. Y. Grama, A. C. T. van Duin, S. A. Pandit, *J. Chem. Phys.* **2010**, *132*, 174704.
[28] J. Yeon, A. C. T. van Duin, *J. Phys. Chem. C* **2016**, *120*, 305.
[29] J. M. Rimsza, J. Yeon, A. C. T. van Duin, J. Du, *J. Phys. Chem. C* **2016**, *120*, 24803.
[30] A. M. Escatllar, P. Ugliengo, S. T. Bromley, *J. Chem. Phys.* **2017**, *146*, 224704.
[31] S. H. Hahn, A. C. T. van Duin, *J. Phys. Chem. C* **2019**, *123*, 15606.
[32] H. J. C. Berendsen, J. P. M. Postma, W. F. van Gunsteren, A. DiNola, J. R. Haak, *J. Chem. Phys.* **1984**, *81*, 3684.
[33] A. Dullweber, B. Leimkuhler, R. McLachlan, *J. Chem. Phys.* **1997**, *107*, 5840.
[34] G. J. Martyna, D. J. Tobias, M. L. Klein, *J. Chem. Phys.* **1994**, *101*, 4177.
[35] W. Shinoda, M. Shiga, M. Mikami, *Phys. Rev. B* **2004**, *69*, 134103.
[36] M. E. Tuckerman, J. Alejandre, R. López-Rendón, A. L. Jochim, G. J. Martyna, A. Liouville-operator, *J. Phys. A: Math. Gen.* **2006**, *39*, 5629.
[37] M. Parrinello, A. Rahman, *J. Appl. Phys.* **1981**, *52*, 7182.
[38] J. Kieffer, A. C. Angell, *J. Non-Cryst. Solids* **1988**, *106*, 336.
[39] A. Nakano, L. Bi, R. K. Kalia, P. Vashishta, *Phys. Rev. B* **1994**, *49*, 9441.
[40] J. V. L. Beckers, S. W. de Leeuw, *J. Non Cryst. Solids* **2000**, *261*, 87.
[41] J. M. Rimsza, J. Du, *J. Am. Ceram. Soc.* **2014**, *97*, 772.
[42] S. Le Roux, P. Jund, *Comput. Mater. Sci.* **2010**, *49*, 70.
[43] D. N. Tafen, D. A. Drabold, *Phys. Rev. B* **2005**, *71*, 054206.
[44] M. Cobb, D. A. Drabold, R. L. Cappelletti, *Phys. Rev. B* **1996**, *54*, 12162.
[45] X. Zhang, D. A. Drabold, *Phys. Rev. B* **2000**, *62*, 15695.
[46] K. Goetzke, H. J. Klein, *J. Non-Cryst. Solids* **1991**, *127*, 215.
[47] X. Yuan, A. N. Cormack, *Comput. Mater. Sci.* **2002**, *24*, 343.
[48] B. Lee, F. Richards, *J. Mol. Biol.* **1971**, *55*, 379.
[49] M. Mantina, A. C. Chamberlin, R. Valero, C. J. Cramer, D. G. Truhlar, *J. Phys. Chem. A* **2009**, *113*, 5806.
[50] A. Stukowski, *Modell. Simul. Mater. Sci. Eng.* **2009**, *18*, 015012.
[51] A. Stukowski, *JOM* **2014**, *66*, 399.

[52] M. Tomozawa, K. M. Davis, *Mater. Sci. Eng. A* **1999**, *272*, 114.

[53] C. N. Liu, B. Ozkaya, S. Steves, P. Awakowicz, G. Grundmeier, *J. Phys. D: Appl. Phys.* **2013**, *46*, 084015.

[54] C. E. Viana, N. I. Morimoto, O. Bonnaud, *Microelectron. Reliab.* **2000**, *40*, 613.

[55] H. Jiang, K. Eyink, J. T. Grant, J. Enlow, S. Tullis, T. J. Bunning, *Chem. Vap. Deposition* **2008**, *14*, 286.

[56] R. Morent, N. De Geyter, S. Van Vlierberghe, P. Dubruel, C. Leys, E. Schacht, *Surf. Coat. Technol.* **2009**, *203*, 1366.

[57] A. Goullet, C. Vallée, A. Granier, G. Turban, *J. Vac. Sci. Technol. A* **2000**, *18*, 2452.

[58] E. Bülbül, D. Hegemann, T. Geue, M. Heuberger, *Coll. Surf. B: Biointerfaces* **2020**, *190*, 110908.

[59] J. Shoeb, M. M. Wang, M. J. Kushner, *J. Vac. Sci. Technol. A* **2012**, *30*, 041303.

[60] J. Shoeb, M. J. Kushner, *J. Vac. Sci. Technol. A* **2012**, *30*, 041304.

[61] D. V. Lopaev, S. M. Zyryanov, A. I. Zotovich, T. V. Rakhimova, Y. A. Mankelevich, E. N. Voronina, *J. Phys. D: Appl. Phys.* **2020**, *53*, 175203.

[62] J. A. Theil, D. V. Tsu, M. W. Watkins, S. S. Kim, G. Lucovsky, *J. Vac. Sci. Technol. A* **1990**, *8*, 1374.

[63] R. Al-Oweini, H. El-Rassy, *J. Mol. Struct.* **2009**, *919*, 140.

[64] E. Bülbül, D. Hegemann, K. Ataka, S. Lehner, J. Heberle, M. Heuberger, *Surf. Interfaces* **2021**, *23*, 100922.

[65] A. M. Wrobel, *J. Macromol. Sci. Chem.* **1985**, *22*, 1089.

[66] K. T. Queeney, M. K. Weldon, J. P. Chang, Y. J. Chabal, A. B. Gurevich, J. Sapjeta, R. L. Opila, *J. Appl. Phys.* **2000**, *87*, 1322.

[67] K. T. Queeney, N. Herbots, J. M. Shaw, V. Atluri, J. Chabal, *Appl. Phys. Lett.* **2004**, *84*, 493.

[68] F. M. Elam, B. C. A. M. van der Velden-Schuermans, S. A. Starostin, M. C. M. van de Sanden, H. W. de Vries, *RSC Adv.* **2017**, *7*, 52274.

[69] A. Brunet-Bruneau, D. Souche, S. Fisson, V. N. Van, G. Vuye, F. Abeles, J. Rivory, *J. Vac. Sci. Technol. A* **1998**, *16*, 2281.

[70] M. R. Alexander, R. D. Short, F. R. Jones, M. Stollenwerk, J. Zabold, W. Michaeli, *J. Mater. Sci.* **1996**, *31*, 1879.

[71] E. Bülbül, P. Rupper, T. Geue, B. Laetitia, M. Heuberger, D. Hegemann, *ACS Appl. Mater. Interfaces* **2019**, *11*, 42760.

[72] A. M. El-Sayed, Y. Wimmer, W. Goes, T. Grasser, V. V. Afanasev, A. L. Shluger, *Phys. Rev. B* **2015**, *92*, 014107.

[73] R. L. Mozzi, B. E. Warren, *J. Appl. Cryst.* **1969**, *2*, 164.

[74] J. R. G. Da Silva, D. G. Pinatti, C. E. Anderson, M. L. Rudee, *Philos. Mag.* **1975**, *31*, 713.

[75] F. Mauri, A. Pasquarello, B. G. Pfrommer, Y.-G. Yoon, S.G. Louie, *Phys. Rev. B* **2000**, *62*, R4786.

[76] M. G. Tucker, D. A. Keen, M. T. Dove, K. Trachenko, *J. Phys.: Condens. Matter* **2005**, *17*, S67.

[77] W. J. Malfait, W. E. Halter, R. Verel, *Chem. Geol.* **2008**, *256*, 269.

[78] T. Galy, M. Marszewski, S. King, Y. Yan, S. H. Tolbert, L. Pilon, *Micropor. Mesopor. Mater.* **2020**, *291*, 109677.

[79] D. Langevin, J. Grenet, J. M. Saiter, *Eur. Polym. J.* **1994**, *30*, 339.

[80] C. Sammon, J. Yarwood, N. Everall, *Polymer* **2000**, *41*, 2521.

[81] C. H. Shen, G. S. Springer, *J. Compos. Mater.* **1976**, *10*, 2.

[82] J. M. Zalc, S. C. Reyes, E. Iglesia, *Chem. Eng. Sci.* **2004**, *59*, 2947.

[83] R. Renou, A. Szymczyk, A. Ghoufi, *J. Chem. Phys.* **2014**, *140*, 044704.

[84] A. Schlaich, E. W. Knapp, R. R. Netz, *Phys. Rev. Lett.* **2016**, *117*, 048001.

[85] R. H. Doremus, *J. Mater. Res.* **1995**, *10*, 2379.

[86] N. Schühler, A. S. da Silva Sobrinho, J. E. Klemberg-Sapieha, M. Andrews, M. R. Wertheimer, *Society of Vacuum Coaters: 39th Annual Technical Conf. Proc.* **1996**, 285.

[87] N. D. Spencer, *Aqueous Lubrication: Natural And Biomimetic Approaches*, World Scientific, India **2014**.

[88] B. W. Chieng, N. A. Ibrahim, W. M. Z. W. Yunus, M. Z. Hussein, *Polymers* **2014**, *6*, 93.

[89] P. J. Blau, *Tribol. Int.* **2005**, *38*, 1007.

[90] D. Hegemann, S. Gaiser, *J. Phys. D: Appl. Phys.* **2022**, *55*, 173002.